Mixed-flow design for microfluidic printing of two-component polymer semiconductor systems

Gang Wang[a,b,c,1], Liang-Wen Feng[b,c,1], Wei Huang[b,c,1], Subhrangsu Mukherjee[d], Yao Chen[b,c], Dengke Shen[b], Binghao Wang[b,c], Joseph Strzalka[e], Ding Zheng[b], Ferdinand S. Melkonyan[b], Jinhui Yan[f], J. Fraser Stoddart[b], Simone Fabiano[b,g], Dean M. DeLongchamp[d,2], Meifang Zhu[a,2], Antonio Facchetti[b,c,h,2], and Tobin J. Marks[b,c,d,2]

[a]State Key Laboratory for Modification of Chemical Fibers and Polymer Materials, International Joint Laboratory for Advanced Fiber and Low-Dimension Materials, College of Materials Science and Engineering, Donghua University, Shanghai 201620, People's Republic of China; [b]Department of Chemistry, Center for Light Energy Activated Redox Processes, Northwestern University, Evanston, IL 60208; [c]Center for Hierarchical Materials Design, Northwestern University, Evanston, IL 60208; [d]Materials Science and Engineering Division, National Institute of Standards and Technology, Gaithersburg, MD 20899; [e]X-Ray Science Division, Argonne National Laboratory, Lemont, IL 60439; [f]Department of Civil and Environmental Engineering, University of Illinois at Urbana–Champaign, Urbana, IL 61801; [g]Laboratory of Organic Electronics, Department of Science and Technology, Linköping University, SE-60174 Norrköping, Sweden; and [h]Flexterra Corporation, Skokie, IL 60077

Contributed by Tobin J. Marks, June 5, 2020 (sent for review February 27, 2020; reviewed by Thuc-Quyen Nguyen and Natalie Stingelin)

The rational creation of two-component conjugated polymer systems with high levels of phase purity in each component is challenging but crucial for realizing printed soft-matter electronics. Here, we report a mixed-flow microfluidic printing (MFMP) approach for two-component π-polymer systems that significantly elevates phase purity in bulk-heterojunction solar cells and thin-film transistors. MFMP integrates laminar and extensional flows using a specially microstructured shear blade, designed with fluid flow simulation tools to tune the flow patterns and induce shear, stretch, and pushout effects. This optimizes polymer conformation and semiconducting blend order as assessed by atomic force microscopy (AFM), transmission electron microscopy (TEM), grazing incidence wide-angle X-ray scattering (GIWAXS), resonant soft X-ray scattering (R-SoXS), photovoltaic response, and field effect mobility. For printed all-polymer (poly[(5,6-difluoro-2-octyl-2H-benzotriazole-4,7-diyl)-2,5-thiophenediyl[4,8-bis[5-(2-hexyldecyl)-2-thienyl]benzo[1,2-b:4,5-b′]dithiophene-2,6-diyl]-2,5-thiophenediyl]) [J51]:(poly{[N,N′-bis(2-octyldodecyl) naphthalene-1,4,5,8-bis(dicarboximide)-2,6-diyl]-alt-5,5′-(2,2′-bithiophene)}) [N2200]) solar cells, this approach enhances short-circuit currents and fill factors, with power conversion efficiency increasing from 5.20% for conventional blade coating to 7.80% for MFMP. Moreover, the performance of mixed polymer ambipolar [poly(3-hexylthiophene-2,5-diyl) (P3HT):N2200] and semiconducting:insulating polymer unipolar (N2200:polystyrene) transistors is similarly enhanced, underscoring versatility for two-component π-polymer systems. Mixed-flow designs offer modalities for achieving high-performance organic optoelectronics via innovative printing methodologies.

mixed-flow design | phase purity | two component | semiconducting polymer | printed electronics

Solution printing is a promising technique for high-throughput, low-cost, industrial-scale manufacturing of organic optoelectronic devices, including circuits and photovoltaic modules (1–3). However, several outstanding challenges center on the limited control of the semiconductor-layer morphology must be addressed to take full advantage of solution printing (4, 5). During the printing process, the (macro-)molecular aggregation and phase separation are tightly coupled to the complexities of ink flow and transport, which include mass transport of solute via convection and diffusion in solution, mass transport of the solvent during evaporation, and heat transfer within and across phase boundaries (1, 6, 7). A significant hurdle in high-throughput solution printing is the timescale mismatch between the aforementioned coupled processes, resulting in nonideal film morphologies. In addition, when utilizing inks with more than one semiconductor as in the case of two-phase systems, as in bulk-heterojunction and bilayer solar cells, transistors, and diodes, phase separation and domain purity greatly affect charge photogeneration efficiency, charge transport, and bimolecular recombination (8–16), all of which have proven challenging to control in device printing (6, 13, 17–21).

Designing microfluidic flow utilizing micropillar-patterned printing blades provides an opportunity to adjust the ordering of the (macro-) molecules and mass transport during the densification/crystallization process, thereby offering an effective morphological control that is directly transferable to large-scale printing (17, 22–24). However, the effects of different blade pattern features and flow design principles remain unclear. Among various fluidic flow types, laminar flow has been demonstrated to align conjugated polymer chains, while extensional flow can induce stretching and conformational changes in semicrystalline conjugated polymer chains (17). In addition and attributable to the rapid mass and heat transfer effects, microfluidic processing strategies have demonstrated superiority in controlling polymer chain stacking and aggregation (17, 22, 23). However, for two-component semiconductor polymer mixtures,

Significance

Blade coating is a promising methodology for the large-scale printing of polymer electronics, affording nonnegligible microstructure control and properties enhancement. Nevertheless, in two-component systems, the optical/electrical/physical properties are largely dominated by phase separation and domain purity phenomena that are challenging to control. Here, we report a mixed-flow microfluidic printing approach to phase purity control, enabled by a printing blade design based on fluid flow simulations. The result is 50% efficiency enhancement for printed all-polymer solar cells vs. conventional printing and similar enhancements for polymer transistors. Mixed flow is a versatile approach to control domain purity in two-component polymeric semiconductor systems and offers a methodology for printing high-performance soft-matter electronics.

Author contributions: G.W., A.F., and T.J.M. designed research; G.W., L.-W.F., W.H., S.M., Y.C., D.S., B.W., J.S., D.Z., J.Y., and S.F. performed research; G.W., S.M., F.S.M., M.Z., A.F., and T.J.M. analyzed data; and G.W., W.H., F.S.M., J.F.S., S.F., D.M.D., M.Z., A.F., and T.J.M. wrote the paper.

Reviewers: T.-Q.N., University of California, Santa Barbara; and N.S., Georgia Institute of Technology.

Competing interest statement: A.F. is founder and Chief Technology Officer of Flexterra Corporation. T.J.M. is a scientific advisor of Flexterra.

[1]G.W., L.-W.F., and W.H. contributed equally to this work.

[2]To whom correspondence may be addressed. Email: dean.delongchamp@nist.gov, zhumf@dhu.edu.cn, a-facchetti@northwestern.edu, or t-marks@northwestern.edu.

This article contains supporting information online at https://www.pnas.org/lookup/suppl/doi:10.1073/pnas.2000398117/-/DCSupplemental.

First published July 9, 2020.

control of domain purity remains unexplored (25–28). Thus, we hypothesized that the rational design of microfluidic channels with special geometries and dimensions, integrating the effects of both laminar and extensional flow to control of polymer chain conformation, would be an attractive printing strategy.

In this work, the mixed-flow printing concept is demonstrated for two-component conjugated polymer systems using integrated laminar and extensional flows, hereafter referred to as MFMP (mixed-flow microfluidic printing), for directing microphase separation, polymer ordering, and domain purity. When used to fabricate all-polymer solar cells (APSCs), the improved morphology affords significantly enhanced short-circuit currents, fill factors, and power conversion efficiencies (PCEs; PCE ~ 6.75 vs. 4.26% for blade coating) for **PTB7-Th** (poly([2,6′-4,8-di(5-ethylhexyl-thienyl)benzo[1,2-b;3,3-b]dithiophene]{3-fluoro-2[(2-ethylhexyl)carbonyl]thieno[3,4-b]thio-phenediyl}):**N2200** (poly{[N,N′-bis(2-octyldodecyl)naphthalene-1,4,5,8-bis(dicarboximide)-2,6-diyl]-alt-5,5′-(2,2′-bithiophene)}) blends. Similarly, a PCE of 7.80% (>50% enhancement vs. the control [5.80%]) is achieved for **J51** (poly[(5,6-difluoro-2-octyl-2H-benzotriazole-4,7-diyl)-2,5-thiophenediyl[4,8-bis[5-(2-hexyldecyl)-2-thienyl]benzo[1,2-b:4,5-b′]dithiophene-2,6-diyl]-2,5-thiophenediyl]):**N2200** APSCs via this mixed-flow printing technique. For polymer thin-film transistors (TFTs), MFMP enhances the mobility of poly(3-hexylthiophene-2,5-diyl) (**P3HT**):**N2200** ambipolar TFTs by two-fold and **N2200**:**PS** (polystyrene) unipolar TFTs by 2.2-fold, demonstrating the versatility of this printing technique for diverse two-component π-polymer devices.

Results and Discussion

Mixed-Flow Blade Design Guided by Simulation. Microfluidic channels of various geometries were evaluated for microfluidic printing of polymer blends using finite element simulations. Flow design concepts were utilized previously for controlling semiconducting film microstructure in organic electronics (1). Among the various flow configurations, laminar flow is known to promote crystallization kinetics, possibly by increasing chain alignment (29), while extensional flow is known to enhance crystallization by stretching the polymer chains (17). Thus, Reichmanis and coworkers (7, 29) utilized laminar flow to align P3HT nanofibers in fabricating high-performance organic thin-film transistors (OTFTs), while Diao and coworkers (1, 17) used extensional flow for large-area coating of aligned small-molecule OTFT arrays, as well as to enhance donor phase crystallinity and contract OSC (organic solar cell) domain size. Note that these pioneering printing studies each utilized a single-flow design. In contrast, MFMP is based on an entirely different concept—mixed flow via integration of laminar and extensional flows.

The effects of fluid flow on polymer phase behavior are well known for commodity polymers and biomolecules (1). Flow-induced nucleation and crystallization are observed in conjugated small molecules and polymers, and are closely related to the flow-induced polymer conformational changes and enhanced mass and heat transfer observed during crystallization. To understand how blade geometry affects velocity changes and flow types in a liquid, finite element fluid simulations were carried out for the blade design shown in Fig. 1*A* and *SI Appendix*. The fluid motion is modeled by incompressible Navier–Stokes equations, given in Eq. **1**:

$$\begin{cases} \rho\left(\frac{\partial \vec{u}}{\partial t} + \vec{u}\cdot\nabla\vec{u} - \vec{g}\right) + \nabla p - 2\mu\Delta\vec{u} = \vec{0} \\ \nabla\cdot\vec{u} = 0, \end{cases} \quad [1]$$

where ρ is the fluid density, μ is dynamic viscosity, $\vec{u}$ is the fluid velocity, p is the pressure, and $\vec{g}$ is gravitational acceleration. An in-house finite element code was utilized to solve the Navier–Stokes equations. As shown in Fig. 1*A* and *SI Appendix*, we chose three typical geometries to modulate the liquid flow: 1) parallel rectangular channels (Fig. 1 *A*, *Left*) and 2) micropillar arrays (Fig. 1 *A*, *Center*) geometries to induce laminar and extensional flows, respectively, and 3) an hourglass-like geometry (Fig. 1 *A*, *Right*) to induce a mixed flow of both laminar and extensional flows. For both the mixed-flow and the extensional flow configurations, recirculation zones are observed between the micropillar gaps, which increase mixing. Finite element fluid simulation details are presented in the *SI Appendix*. For the mixed-flow configuration, we hypothesize that the high extensional strain

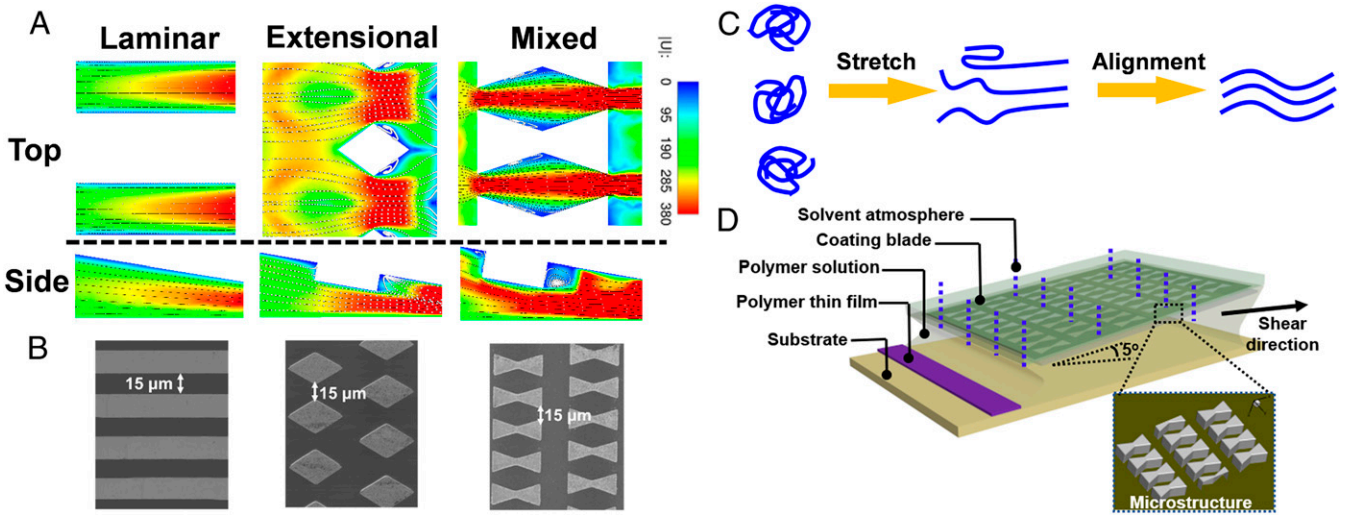

Fig. 1. Blade design and process for controlling semiconducting polymer film microstructure. (*A*) Finite element fluid simulations (streamline representation) of the flow field between microstructured printing blades and the substrate, affording the indicated flow patterns. Note that |U| is the fluid velocity in micrometers per second. (*B*) Blade scanning electron microscopes (SEM) images with microstructures fabricated according to the fluid simulation results. (*C*) Polymer conformational change schematic in the shear field. (*D*) Microfluidic printing process schematic implemented in a solution shearing platform. The black arrow indicates the coating direction, and the contact angle between the substrate and coating blade is ~5°. *Inset* shows the silicon coating blade microstructure designed to induce mixed flow.

rate facilitates stretching of the polymer chains, which are subsequently aligned under the laminar flow, as exemplified in Fig. 1*C* and *SI Appendix*. Both effects cooperate to promote polymer aggregation and in the case of polymer–polymer blends, drive microphase separation between the two polymers. The unique hourglass-like geometry may also induce pushout effects (30, 31) to promote pure domain formation.

To validate the microfluidic printing methodology proposed here, patterned silicon blades were fabricated using photolithography and reactive ion etching (details in the *SI Appendix, Materials and Methods*). The patterned blades were subsequently functionalized with an *n*-octadecyl trichlorosilane monolayer to minimize polymer deposition during the printing process. As shown in Fig. 1*B* and *SI Appendix*, microfluidic printing blades with parallel rectangular channels (Fig. 1 *B*, *Left*), the micropillar arrays (Fig. 1 *B*, *Center*), and the microhourglass arrays (Fig. 1 *B*, *Right*) were fabricated to induce the laminar flow (microfluidic printing [MP]-laminar), extensional flow (MP-extensional), and mixed flow (MFMP), respectively. The gap between the neighboring microstructural elements was fixed at ∼15 μm, all having a depth of 20 μm, controlled by the etching time. Semiconductor solution printing was carried out by integrating the blade with a moving stage (Fig. 1*D* and *SI Appendix*), printing at rates of 20 to 200 μm/s. A 50-μL volume of solution was dispensed on the substrate; the blade was next contacted to the substrate, forming an angle of 5°; and the liquid was printed. During the printing process, the printer head was maintained inside a confined box to create a solvent atmosphere. A photograph of the equipment is provided in *SI Appendix*, Fig. S1, and fabricated blade microstructure characterization data are provided in *SI Appendix*, Figs. S2–S4. Printing experimental details are provided in *SI Appendix, Materials and Methods*. Control printing experiments were carried out with a featureless conventional blade and with MP blades providing laminar, extensional, and mixed flows.

MFMP Printing of APSC Semiconductor Blends. To compare MFMP with other printing techniques for APSCs, cells based on the donor:acceptor blend **PTB7-Th** (number-average molecular weight (*M*n) = 25 kDa):**N2200** (*M*n = 36 kDa) were fabricated (*SI Appendix* has details). These polymers were selected because extensive literature reports optimized PCEs of 4.5 to 5.0% (32, 33). An inverted device architecture of indium tin oxides (ITO)/ZnO (25 nm)/**PTB7-Th**:**N2200**/molybdenum(VI) oxide (MoO_x) (10 nm)/Ag (100 nm) was utilized (Fig. 2*A* and *SI Appendix*). Representative current density–voltage (*J–V*) curves under air mass (AM) 1.5-global (G) (100 mW/cm^2) illumination are shown in Fig. 2*B* and *SI Appendix*, and performance data are summarized in Table 1 and *SI Appendix*. In preliminary experiments, it is found that the film morphology changes with the coating speed, increasing it from 20 to 200 μm/s. The AFM images of the film printed at various coating speeds can be found in *SI Appendix*, Fig. S5. PCE maximizes at speeds of ∼100 μm/s, a factor mostly related to optimizing the photoactive-layer film thickness at an optimum ∼100 nm.

Note from Table 1 and *SI Appendix* that the APSCs fabricated by the MFMP methodology exhibit the highest PCE of 6.75% along with the highest J_{SC} = 14.32 mA/cm^2 and fill factor (*FF*) = 54.5%. In contrast, control devices fabricated using conventional blade coating in the same apparatus (indicated as blade coating) exhibit the lowest PCE (4.26%) and other metrics. APSCs fabricated by MP-laminar yield PCE = 4.97% and other metrics below those of the MFMP devices. The same is true of the MP-extensional devices. Note that the very small variation in V_{OC} is consistent with constant orbital energetics. The external quantum efficiency (EQE) spectra of the APSCs in Fig. 2*C* and *SI Appendix* corroborate the *J–V* measurement performance data. Together, these results show that the MFMP printing technique affords superior APSC performance. The PCE enhancement (∼55%) vs. blade coating is mainly the result of the increased J_{SC} (∼30%) and *FF* (∼17%). In addition, an excellent PCE of 7.80% is achieved for donor **J51** (*M*n = 11 kDa):**N2200** (*M*n = 46 kDa) acceptor APSCs printed by the MFMP technique vs. 5.80% for blade coating (*SI Appendix*, Fig. S6; details are in *SI Appendix*). A PCE ∼ 7% is considered sufficient for market introduction (34, 35), and integration of the present mixed-flow printing with roll-to-roll solution fabrication processes would then enable OSC manufacture.

Next, vertical charge transport in the **PTB7-Th**:**N2200** active-layer blend films fabricated by various processing methods was probed by space–charge-limited current measurements using

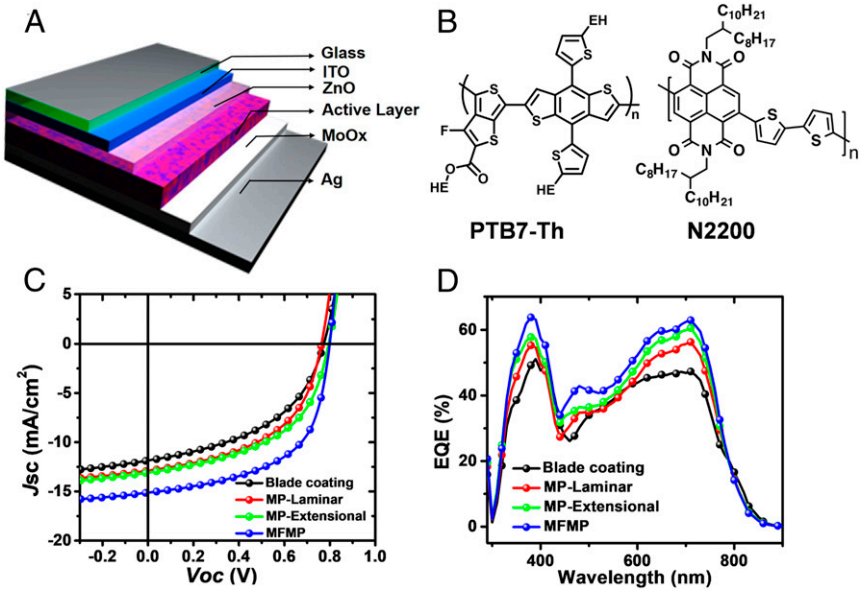

Fig. 2. Comparison of APSC performance for blade coating and synergistic flow printing of the indicated pattern features. (*A*) Schematic representation of APSC architecture. Ag is the abbreviation of silver. (*B*) Chemical structures of the polymer donor **PTB7-Th** and acceptor **N2200** used in this study. (*C*) *J–V* characteristics of the APSCs fabricated with the indicated techniques. (*D*) Corresponding EQE spectra.

Table 1. PTB7-Th:N2200 polymer solar cells photovoltaic and mobility parameters

Processing	V_{OC} (V)	J_{SC} (mA/cm^2)	*FF* (%)	PCE (%)	μ_h	μ_e
Blade coating	0.77 ± 0.01	11.85 ± 1.25	46.73 ± 4.15	4.26 (4.50)	2.35 ± 0.27	3.01 ± 0.35
MP-laminar	0.76 ± 0.01	12.89 ± 1.45	50.75 ± 5.46	4.97 (5.20)	3.25 ± 0.33	5.31 ± 0.32
MP-extensional	0.79 ± 0.01	13.08 ± 1.55	51.13 ± 3.25	5.30 (5.60)	3.88 ± 0.24	5.20 ± 0.46
MFMP	0.80 ± 0.01	14.32 ± 1.45	54.47 ± 4.23	6.30 (6.75)	4.60 ± 0.32	6.98 ± 0.70

Donor:acceptor weight ratio = 1:1. Values are averages of eight devices. Values in parentheses are highest PCEs; μ_h and μ_e are given in $10^{-5}\times$ (centimeters^2 per Vs).

diodes of structure ITO/ZnO/active layer/LiF/Al (electron only) and ITO/MoO_x/active layer/MoO_x/Ag (hole only). Mobilities (Table 1 and *SI Appendix*) were extracted by fitting the *J–V* curves using the Mott–Gurney relationship (36). Importantly, compared with the conventional fabrication methods (blade coating, MP-laminar, and MP-extensional), the films fabricated by the MFMP printing exhibit enhanced and balanced hole (μ_h) and electron (μ_e) mobilities of 4.60×10^{-5} and 6.98×10^{-5} cm^2/voltage second (Vs), respectively, which can be generally attributed to the enhanced crystallinity, proper phase separation, and high phase purity (vide infra) (37, 38).

Printing Effects on Blend Film Morphology. The present APSC blend film morphologies were first investigated by TEM and AFM. TEM images in Fig. 3 *A–D* and *SI Appendix*, Fig. S7 indicate that, compared with films fabricated by blade coating, MP-laminar, and MP-extensional printing, the MFMP films exhibit nanoscale phase separation, with bicontinuous interpenetrating networks clearly observable. Nevertheless, owing to density variations and differing surface roughness, unambiguous extraction of domain sizes proved challenging. Thus, R-SoXS (resonant soft X-ray scattering) was used to quantify domain size and purity (vide infra). AFM images are also shown in Fig. 3 *A*, *Inset*, *B*, *Inset*, *C*, *Inset*, and *D*, *Inset* and *SI Appendix*, and further details can be found in *SI Appendix*, Fig. S8. From the AFM characterization, the MFMP printed films exhibit relatively small fibril aggregates and significantly fine microstructure, which is expected to provide continuous and efficient pathways for both exciton splitting and carrier transport.

To further investigate blend film microstructure, GIWAXS (grazing incidence wide-angle X-ray scattering) data were taken, and details are presented in Fig. 3 *E–H* and *SI Appendix*. Both in-plane/out-of-plane line cuts and pole-figure plots extracted from the lamellar diffraction are shown in *SI Appendix*, Figs. S9 and S10. The ordering in the blend films is mainly related to the acceptor polymer **N2200** since the donor polymer **PTB7-Th** remains amorphous (or has low crystallinity) under all printing conditions. The sample volume normalized relative diffraction strengths obtained from integration of pole figures (*SI Appendix*, Fig. S10) for the different samples are: blade coating (~0.60), MP-laminar (~0.61) < MP-extensional (~0.99) ~ MFMP (~1). In addition, it is found that all of the samples fabricated by various printing techniques exhibit preferential face-on distributions from the pole figures extracted from the lamellar diffraction. The (100) lamella stacking distance falls from 24.56 to 24.38 to 24.20 Å and to 23.90 Å when the processing changes from blade coating to MP-laminar to MP-extensional and to MFMP, respectively. In addition, the (010) π–π stacking distance

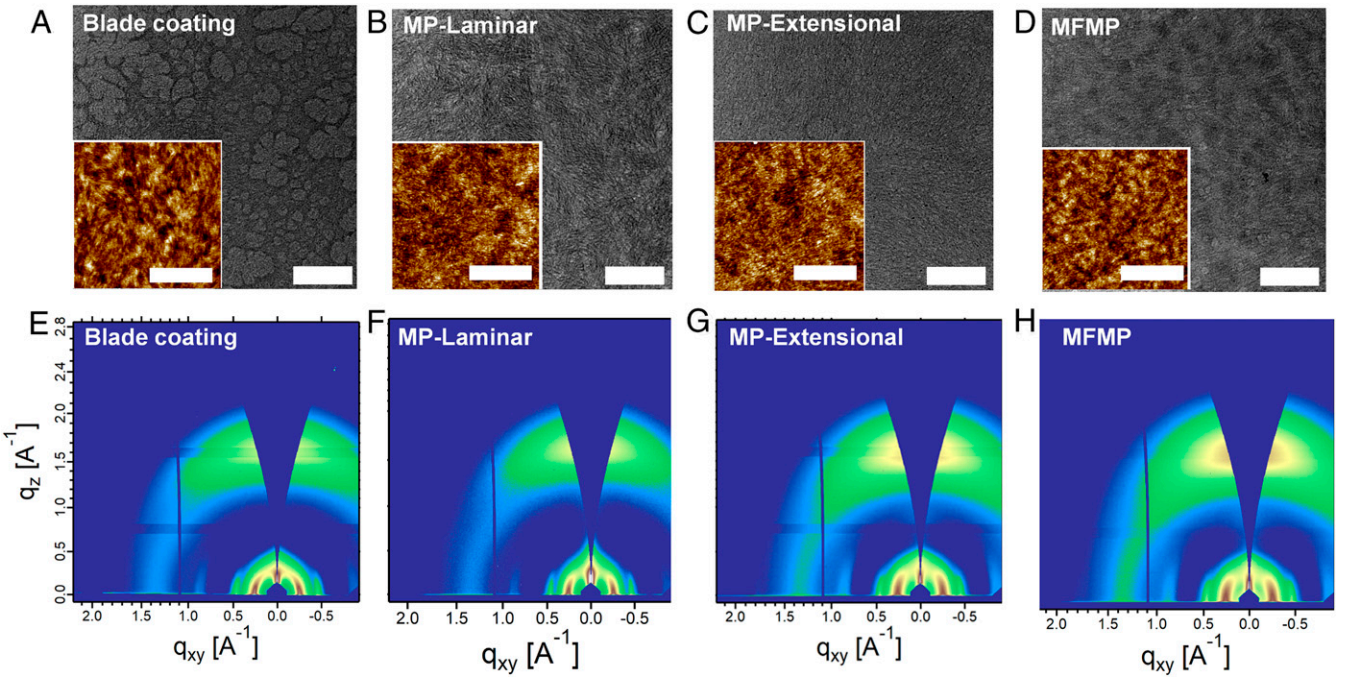

Fig. 3. Morphological and microstructural analysis of the blend films fabricated with the indicated printing methods. (*A–D*) TEM characterization of APSC films created via the various printing methods with (*Insets*) corresponding AFM phase images: (*A*) blade coating, (*B*) MP-laminar, (*C*) MP-extensional, and (*D*) MFMP. (Scale bars: *A–D*, 100 nm; *Insets*, 200 nm.) (*E–H*) GIWAXS patterns (same color scale) of APSC films created via the various printing methods: (*E*) blade coating, (*F*) MP-laminar, (*G*) MP-extensional, and (*H*) MFMP.

is only 3.79 Å for MFMP-printed films, while it is considerably larger for the other printing processes: 3.95, 3.90, and 3.85 Å for blade coating, MP-laminar, and MP-extensional, respectively (summarized in *SI Appendix*, Table S1). These results argue that mixed-flow printing promotes the most closely packed side chains as well as closely stacked backbones compared with the other methods.

Domain Purity Analysis and Proposed Printing Mechanism. R-SoXS was carried out to obtain a more complete picture of the blend film morphology—the characteristic size scales and relative in-plane spatial distribution and composition variations or purity variations over length scales spanning ~10 to 1,000 nm. A representative two-dimensional (2D) R-SoXS image of the APSC bulk-heterojunction films prepared via the MFMP process is shown in Fig. 4*A* and *SI Appendix*. The detailed information and discussion concerning the R-SoXS profiles acquired at different energies and peak fitting can be found in *SI Appendix*, Figs. S11–S15 and Table S2. As shown in Fig. 4*B* and Figs. S11-S15 in the *SI Appendix*, all films prepared by the various fabrication methods exhibit relatively similar median domain sizes of 131 nm (blade coating), 131 nm (MP-laminar), 125 nm (MP-extensional), and 126 nm (MFMP). The domain size distributions are broad, and there appear to be minority populations of smaller dimensions (*SI Appendix*, Fig. S12). Significantly, as plotted in Fig. 4*C*, large differences in domain purity are observed for the films fabricated via various processing methods. The normalized domain purity is 0.66, 0.82, 0.74, and 1.0 for blade coating, MP-laminar, MP-extensional, and MFMP, respectively. Impressively, the mixed-flow printing achieves the highest domain purity. Regarding APSC photovoltaic performance, note that both *FF* and J_{SC} trends track the domain purity trends calculated over the entire q range as seen in *SI Appendix*, Figs. S11–S14.

The combined morphological and microstructural data presented here clearly demonstrate that MFMP fabrication enhances APSC J_{SC} (+30%) and *FF* (+17%), which can be attributed to the higher degree of **N2200** ordering and more importantly, increased domain purity that reduces nongeminate charge carrier recombination by enhancing charge transport. Furthermore, the higher crystallinity and increased purity at smaller length scales corresponding to peaks 2 and 3 (*SI Appendix*) of the acceptor polymer phase are expected to facilitate charge generation within the exciton diffusion length for efficient dissociation and to mitigate recombination. All these factors combined lead to a pronounced increase in PCE (+55%).

Based on the combined fluid flow simulations, microstructure analysis, photophysical properties, charge transport, and domain purity results, we propose the following printing scenario in Fig. 4*D* and *SI Appendix* for mixed-flow enhanced domain purity.

Stage I: Polymer conformational rearrangement. Extensional and shear flows stretch the polymer chains, reducing coil defects as well as interchain entanglements (39, 40).

Stage II: Polymer chain alignment. Under laminar flow, the stretched chains are aligned, which decreases the aggregation/crystallization entropy (41).

Stage III: Pure phase formation of aggregates/crystals. The aligned polymer chains begin to aggregate, eventually forming larger highly pure aggregated/ordered domains (42, 43).

Fig. 4*E* and *SI Appendix* show a schematic depiction of the blend morphologies. Compared with other printing techniques, the high domain purity and enhanced crystallinity of the MFMP mixed blend suppress geminate recombination and reduce the bimolecular charge recombination, leading to the enhanced charge transport, and collection, thereby enhancing J_{SC} and FF (44, 45).

Versatility: TFTs. To test the broader applicability of the MFMP process in optimizing the film morphology of other two-component semiconductor systems, we fabricated OTFTs using the classical **P3HT**:**N2200** ambipolar and the **N2200**:**PS** blends as model systems. The chemical structures of **P3HT**, **N2200,** and **PS** are shown in Fig. 5*A* and *SI Appendix*. Bottom-gate/bottom-contact TFTs were fabricated using spin coating, blade coating, and MFMP using a **P3HT**:**N2200** blend solution (10 mg/mL in xylene, with the mass ratio of 1:1). The resulting μ_h and μ_e values are ~(0.003 and 0.003) cm^2/Vs, (0.0042 and 0.0045) cm^2/Vs, and (0.0056 and 0.0058) cm^2/Vs, respectively (Fig. 5 *B*, *Right*). From previous reports, enhanced phase separation with percolating pathways parallel to the substrate promotes ambipolarity (46).

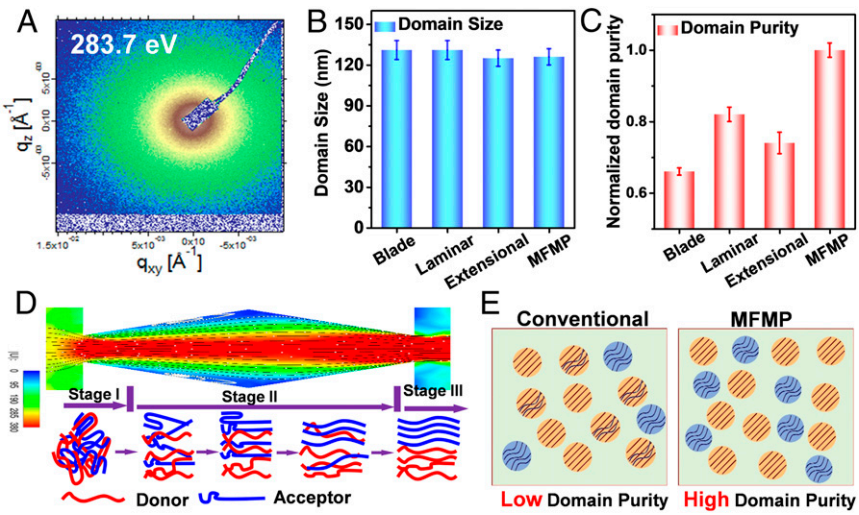

Fig. 4. Domain purity analysis of **PTB7-Th**:**N2200** APSC films fabricated by the indicated printing methods. (*A*) The 2D R-SoXS image of films fabricated by MFMP printing. Intensity is plotted on a log scale, with white, brown, yellow, and green ranging from high to low intensities. Variation of (*B*) domain size and (*C*) domain purity obtained from integration of R-SoXS peaks that reflect material contrast. Uncertainty bars estimated from peak fits to profiles acquired at several energies in the range from 283 to 284 eV where material contrast is optimum. (*D*) Model of polymer conformational change, alignment, and pure domain formation in a shear field. (*E*) Schematic illustration of possible in-plane morphology (simplified to focus on domain purity/crystallinity information).

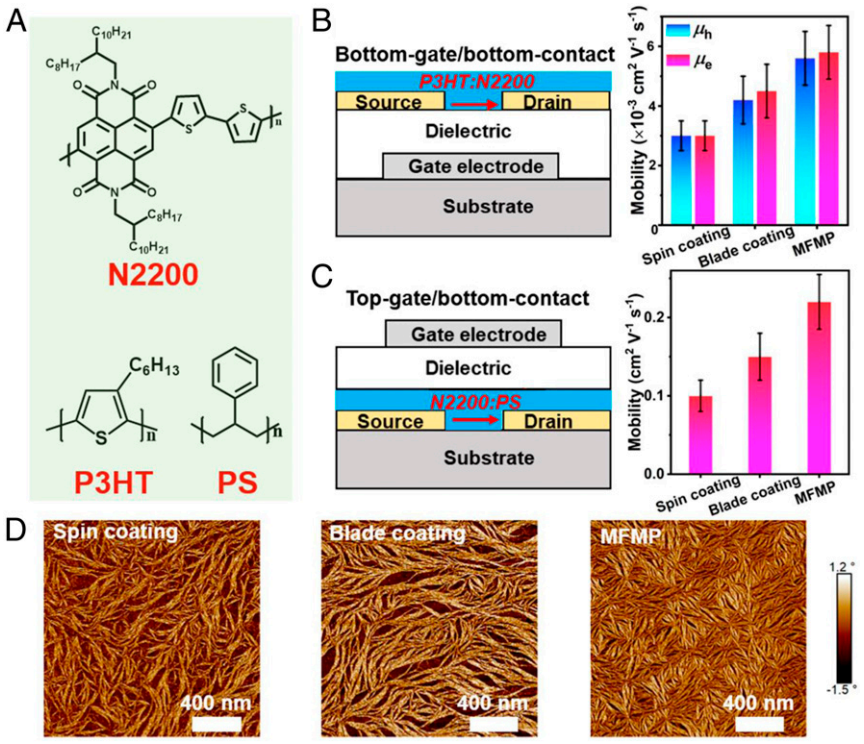

Fig. 5. Versatility of mixed-flow printing for two-component conjugated polymer transistor systems. (*A*) Chemical structures of **N2200**, **P3HT**, and **PS**. (*B*, *Left*) Device architecture of bottom-gate/bottom-contact transistor for **P3HT**:**N2200** blend films and (*B*, *Right*) corresponding charge transport mobility summary using the indicated printing methods. (*C*, *Left*) Device architecture of the top-gate/bottom-contact transistors (*Left*) for **N2200**:**PS** blend films and (*C*, *Right*) corresponding mobility summary using the indicated printing methods. (*D*) AFM images of the **N2200**:**PS** blend films.

Here, the highest mobilities achieved by the mixed-flow design strategy can be attributed to crystalline and pure conductive channels.

Finally, this approach was evaluated for the semiconductor–insulator **N2200**:**PS** blend system using a top-gate, bottom-contact TFT architecture (Fig. 5 *C*, *Left* and *SI Appendix*). The blend was deposited using 8 mg/mL in dichlorobenzene solutions, with the mass ratio of 95:5 for **PS**:**N2200**. The mobility is normalized for the actual channel area. The resulting μ_e is ~(0.10, 0.15, and 0.22) cm^2/Vs for spin coating, blade coating, and mixed-flow printing, respectively (Fig. 5*C* and *SI Appendix*). The X-ray photoelectron spectroscopy (XPS) depth-profiling results suggest that the top layer is exclusively **N2200** and the bottom layer is **PS**. From the AFM image (Fig. 5*D* and *SI Appendix*), the MFMP printing films are fully covered by **N2200** fibrils, in accord with enhanced vertical phase separation and pure domains compared with the blade coating and spin coating methods (47, 48). The above results underscore the favorable generality of the mixed-flow printing concept for two-component polymer transistor systems.

Conclusions

A "mixed-flow design" strategy for microfluidic printing is demonstrated for two-component semiconducting conjugated polymer systems with application to organic optoelectronic devices. Fluid simulations are utilized to design an optimum printing blade topology, which integrates laminar and extensional flows for semiconductor blend printing. APSCs fabricated with **PTB7-Th**:**N2200** blends exhibit increased donor/acceptor phase separation and phase purity due to the pushout effects of the mix-flow blade microstructure and synergistic effects of both laminar and extensional flows. The improved blend morphology leads to higher J_{SC} together with enhanced FF and >50% increase in PCE vs. conventional blade coating. Also, an impressive PCE of 7.80% can be achieved for the **J51**:**N2200** system via mixed-flow printing. In addition, this printing technique also enhances charge transport for **P3HT**:**N2200** and **N2200**:**PS** blend OTFTs, implying a significant versatility for two-component conjugated polymer systems. Thus, mixed-flow printing is an effective methodology for printing high-performance soft-matter electronics.

Methods

For the microstructure-patterned blade fabrication, standard photolithographic techniques were utilized, followed by reactive ion etching. As illustrated in Fig. 1*A*, the microstructure-patterned blade was positioned ~20 μm above the glass substrate and maintained under a chlorobenzene vapor atmosphere. The fabricated films were characterized by AFM, TEM, GIWAXS, and R-SoXS. Solar cells were fabricated using PTB7-Th:N2200 bulk-heterojunction blends, while transistors were fabricated with the N2200:PS and P3HT:N2200 materials systems. More detailed information is provided in *SI Appendix*.

Data Availability. All data are available in the text and *SI Appendix*.

ACKNOWLEDGMENTS. This research was supported in part by the Center for Light Energy Activated Redox Processes, an Energy Frontier Research Center funded by the US Department of Energy (DOE), Office of Science, Office of Basic Energy Sciences under Award DE-SC0001059; US Department of Commerce, National Institute of Standards and Technology Award 70NANB14H012 as part of the Center for Hierarchical Materials Design; Air Force Office of Scientific Research (AFOSR) Grant FA9550-18-18-1-0320; and Office of Naval Research Contract N00014-20-1-2116. Use of the Advanced Photon Source, an Office of Science User Facility operated for the US DOE Office of Science by Argonne National Laboratory, was supported by the US DOE under Contract DE-AC02-06CH11357. R-SoXS data were acquired at beamline 11.0.1.2 at the Advanced Light Source, which is supported by the Director, Office of Science, Office of Basic Energy Sciences of the US DOE under Contract DE-AC02-05CH11231. This work made use of the Electron Probe Instrumentation Center (EPIC), Keck Interdisciplinary Surface Science facili (Keck-II), and/or Scanned Probe Imaging and Development (SPID)

facilities of Northwestern University's Northwestern University Atomic and Nanoscale Charaterization Experimental (NUANCE) Center, which has received support from the Soft and Hybrid Nanotechnology Experimental Resource (NSF Grant NNCI-1542205); the Materials Research Science and Engineering Centers (MRSEC) program (NSF Grant DMR-1121262) at the Materials Research Center; the International Institute for Nanotechnology (IIN); the Keck Foundation; and the State of Illinois through the IIN. G.W. is grateful for financial support from the Program for Professors of Special Appointment (Eastern Scholar) at Shanghai Institutions of Higher Learning, the Fundamental Research Funds for the Central Universities, the Young Elite Scientists Sponsorship Program by China Association for Science and Technology (CAST), and Natural Science Foundation of Shanghai Grant 19ZR1470900. L.-W.F. thanks Shanghai Institute of Organic Chemistry and Jiangsu Aosaikang Pharmaceutical Co., Ltd. for a postdoctoral fellowship. S.F. received financial support from the Swedish Governmental Agency for Innovation Systems (VINNOVA) Grant 2015-04859 and Swedish Research Council Grant 2016-03979. M.Z. is grateful for financial support from National Natural Science Foundation of China Grant 51733002 and Innovation Program of Shanghai Municipal Education Commission Grant E0055. C. Wang of the Advanced Light Source (ALS) (DOE) is acknowledged for assisting with the experimental setup and providing instrument maintenance. The manuscript was written through contributions of all authors. All authors have given approval to the final version of the manuscript.

1. G. Qu, J. J. Kwok, Y. Diao, Flow-directed crystallization for printed electronics. *Acc. Chem. Res.* **49**, 2756–2764 (2016).
2. K. Hwang *et al*., Toward large scale roll-to-roll production of fully printed perovskite solar cells. *Adv. Mater.* **27**, 1241–1247 (2015).
3. R. Po *et al*., From lab to fab: How must the polymer solar cell materials design change? An industrial perspective. *Energy Environ. Sci.* **7**, 925–943 (2014).
4. H. Azimi, Y. Hou, C. J. Brabec, Towards low-cost, environmentally friendly printed chalcopyrite and kesterite solar cells. *Energy Environ. Sci.* **7**, 1829–1849 (2014).
5. M. He *et al*., Meniscus-assisted solution printing of large-grained perovskite films for high-efficiency solar cells. *Nat. Commun.* **8**, 16045 (2017).
6. M. Liu *et al*., Fused perylene diimide-based polymeric acceptors for efficient all-polymer solar cells. *Macromolecules* **50**, 7559–7566 (2017).
7. N. E. Persson, P.-H. Chu, M. McBride, M. Grover, E. Reichmanis, Nucleation, growth, and alignment of poly(3-hexylthiophene) nanofibers for high-performance OFETs. *Acc. Chem. Res.* **50**, 932–942 (2017).
8. W. Huang *et al*., Isolating and quantifying the impact of domain purity on the performance of bulk heterojunction solar cells. *Energy Environ. Sci.* **10**, 1843–1853 (2017).
9. C. Duan *et al*., The role of the axial substituent in subphthalocyanine acceptors for bulk-heterojunction solar cells. *Angew. Chem. Int. Ed. Engl.* **56**, 148–152 (2017).
10. X. Guo *et al*., Polymer solar cells with enhanced fill factors. *Nat. Photonics* **7**, 825–833 (2013).
11. H. Zhang *et al*., Improved domain size and purity enables efficient all-small-molecule ternary solar cells. *Adv. Mater.* **29**, 1703777 (2017).
12. B. Fan *et al*., All-polymer solar cells based on a conjugated polymer containing siloxane-functionalized side chains with efficiency over 10. *Adv. Mater.* **29**, 1703906 (2017).
13. L. Ye *et al*., Precise manipulation of multilength scale morphology and its influence on eco-friendly printed all-polymer solar cells. *Adv. Funct. Mater.* **27**, 1702016 (2017).
14. S. Mukherjee, C. M. Proctor, G. C. Bazan, T.-Q. Nguyen, H. Ade, Significance of average domain purity and mixed domains on the photovoltaic performance of high-efficiency solution-processed small-molecule BHJ solar cells. *Adv. Energy Mater.* **5**, 1500877 (2015).
15. S. Mukherjee, X. Jiao, H. Ade, Charge creation and recombination in multi-length scale polymer:fullerene BHJ solar cell morphologies. *Adv. Energy Mater.* **6**, 1600699 (2016).
16. L. Ye *et al*., High-efficiency nonfullerene organic solar cells: Critical factors that affect complex multi-length scale morphology and device performance. *Adv. Energy Mater.* **7**, 1602000 (2017).
17. Y. Diao *et al*., Flow-enhanced solution printing of all-polymer solar cells. *Nat. Commun.* **6**, 7955 (2015).
18. S. Pröller *et al*., Following the morphology formation in situ in printed active layers for organic solar cells. *Adv. Energy Mater.* **6**, 1501580 (2016).
19. N. Li, C. J. Brabec, Air-processed polymer tandem solar cells with power conversion efficiency exceeding 10%. *Energy Environ. Sci.* **8**, 2902–2909 (2015).
20. W. Zhao *et al*., Environmentally friendly solvent-processed organic solar cells that are highly efficient and adaptable for the blade-coating method. *Adv. Mater.* **30**, 1704837 (2018).
21. H. W. Ro *et al*., Morphology changes upon scaling a high-efficiency, solution-processed solar cell. *Energy Environ. Sci.* **9**, 2835–2846 (2016).
22. Y. Diao *et al*., Solution coating of large-area organic semiconductor thin films with aligned single-crystalline domains. *Nat. Mater.* **12**, 665–671 (2013).
23. Y. Diao, L. Shaw, Z. Bao, S. C. B. Mannsfeld, Morphology control strategies for solution-processed organic semiconductor thin films. *Energy Environ. Sci.* **7**, 2145–2159 (2014).
24. G. Wang *et al*., Aggregation control in natural brush-printed conjugated polymer films and implications for enhancing charge transport. *Proc. Natl. Acad. Sci. U.S.A.* **114**, E10066–E10073 (2017).
25. A. Mahajan *et al*., A self-aligned strategy for printed electronics: Exploiting capillary flow on microstructured plastic surfaces. *Adv. Electron. Mater.* **1**, 1500137 (2015).
26. X. Yu, W. Shou, B. K. Mahajan, X. Huang, H. Pan, Materials, processes, and facile manufacturing for bioresorbable electronics: A review. *Adv. Mater.* **30**, e1707624 (2018).
27. X. Gu *et al*., Roll-to-roll printed large-area all-polymer solar cells with 5% efficiency based on a low crystallinity conjugated polymer blend. *Adv. Energy Mater.* **7**, 1602742 (2017).
28. X. Gu, L. Shaw, K. Gu, M. F. Toney, Z. Bao, The meniscus-guided deposition of semiconducting polymers. *Nat. Commun.* **9**, 534 (2018).
29. G. Wang *et al*., Microfluidic crystal engineering of π-conjugated polymers. *ACS Nano* **9**, 8220–8230 (2015).
30. G. Xin *et al*., Microfluidics-enabled orientation and microstructure control of macroscopic graphene fibres. *Nat. Nanotechnol.* **14**, 168–175 (2019).
31. M. Trebbin *et al*., Anisotropic particles align perpendicular to the flow direction in narrow microchannels. *Proc. Natl. Acad. Sci. U.S.A.* **110**, 6706–6711 (2013).
32. G. Wang, F. S. Melkonyan, A. Facchetti, T. J. Marks, All-polymer solar cells: Recent progress, challenges, and prospects. *Angew. Chem. Int. Ed. Engl.* **58**, 4129–4142 (2019).
33. G. Wang *et al*., Photoactive blend morphology engineering through systematically tuning aggregation in all-polymer solar cells. *Adv. Energy Mater.* **8**, 1702173 (2018).
34. H. Kang *et al*., Bulk-heterojunction organic solar cells: Five core technologies for their commercialization. *Adv. Mater.* **28**, 7821–7861 (2016).
35. S. Berny *et al*., Solar trees: First large-scale demonstration of fully solution coated, semitransparent, flexible organic photovoltaic modules. *Adv. Sci. (Weinh.)* **3**, 1500342 (2015).
36. S. Foster *et al*., Electron collection as a limit to polymer:PCBM solar cell efficiency: Effect of blend microstructure on carrier mobility and device performance in PTB7:PCBM. *Adv. Energy Mater.* **4**, 1400311 (2014).
37. L. Ye *et al*., Manipulation of domain purity and orientational ordering in high performance all-polymer solar cells. *Chem. Mater.* **28**, 6178–6185 (2016).
38. Z. Li *et al*., High performance all-polymer solar cells by synergistic effects of fine-tuned crystallinity and solvent annealing. *J. Am. Chem. Soc.* **138**, 10935–10944 (2016).
39. C. M. Schroeder, H. P. Babcock, E. S. G. Shaqfeh, S. Chu, Observation of polymer conformation hysteresis in extensional flow. *Science* **301**, 1515–1519 (2003).
40. S. Moghadam, I. Saha Dalal, R. G. Larson, Unraveling dynamics of entangled polymers in strong extensional flows. *Macromolecules* **52**, 1296–1307 (2019).
41. Z. Wang, Z. Ma, L. Li, Flow-induced crystallization of polymers: Molecular and thermodynamic considerations. *Macromolecules* **49**, 1505–1517 (2016).
42. B. A. Wolf, Thermodynamic theory of flowing polymer solutions and its application to component separation. *Macromolecules* **17**, 615–618 (1984).
43. H. Tanaka, T. Araki, Component inversion during viscoelastic component separation: Roles of bulk and shear relaxation moduli. *Phys. Rev. Lett.* **78**, 4966–4969 (1997).
44. D. Credgington, F. C. Jamieson, B. Walker, T. Q. Nguyen, J. R. Durrant, Quantification of geminate and non-geminate recombination losses within a solution-processed small-molecule bulk heterojunction solar cell. *Adv. Mater.* **24**, 2135–2141 (2012).
45. C. Proctor, D. Neher, T. Q. Nguyen, Overcoming geminate and enhancing extraction in solution-processed small molecule solar cells. *Adv. Energy Mater.* **4**, 1400230 (2014).
46. S. Fabiano *et al*., Charge transport orthogonality in all-polymer blend transistors, diodes, and solar cells. *Adv. Energy Mater.* **4**, 1301409 (2013).
47. S. Wang *et al*., Experimental evidence that short-range intermolecular aggregation is sufficient for efficient charge transport in conjugated polymers. *Proc. Natl. Acad. Sci. U.S.A.* **112**, 10599–10604 (2015).
48. L. Bu, M. Hu, W. Lu, Z. Wang, G. Lu, Printing semiconductor-insulator polymer bilayers for high-performance coplanar field-effect transistors. *Adv. Mater.* **30**, 1704695 (2018).